Image Reconstruction from Sparse Irregular Intensity Interferometry Measurements of Fourier Magnitude

David R. Gerwe, J. J. Dolne
Boeing Phantomworks Space & Intelligence Systems
Peter N. Crabtree
United States Air Force Research Labs
Richard B. Holmes, Brandoch Calef
Boeing Laser and Technical Services

ABSTRACT

A forward model-based algorithm for reconstructing images from Fourier domain measurements is described. The model accurately treats broadening of the Fourier domain sampling function resulting from finite aperture size and spectral bandwidth. The forward modeling approach also allows weighting of measurements according to their individual signal-to-noise ratios (SNRs), and injection of *a priori* expectations about the object such as its support and power spectral density. Image quality performance of a large telescope array is analyzed as a function of SNR and array scale. The approach is designed to enable joint processing of mixtures of intensity and amplitude interferometric measurements and conventional incoherent images, but the focus of this paper is limited to intensity interferometry. Basic structures of the object are seen to be recovered as SNR approaches 10 for unity coherence.

1. INTRODUCTION

Intensity interferometry was proposed in the mid-1950s by Hanbury Brown and Twiss in the mid 1950s [1-3]. Over the ensuing decades, the concept was developed into an instrument that successfully measured the widths of a number of stars, and has also been applied to other fields outside of astronomy [4-8]. Emphasis later shifted away from intensity interferometry as it became apparent that amplitude interferometry had better signal-to-noise ratio (SNR) and image formation capabilities, especially in view of improved optical technologies such as adaptive optics [9-11]. In addition to SNR, image formation has been a question for intensity interferometry. Intrinsic ambiguities were present in reconstructions of amplitude-only data from conventional approaches such as phase retrieval [12-13]. However, a number of techniques were developed to retrieve an image that worked under high-SNR conditions [14-19].

In order to address performance under low SNR conditions, new approaches have been developed including forward model-based techniques [20-22]. A forward model is a set of mathematical relations that relate the pristine object, sensor design, and environmental conditions to the measurements. A forward model in image reconstruction involves estimating the object that when propagated through the forward model best fits the data in terms of some cost function, subject to various constraints and *a priori* expectations, for example non-negativity, support, entropy, total variation, image sharpness, and prior knowledge. In the most rigorous case the quality of fit to the data is quantified by its likelihood according to a physics-based model of the measurement noise statistics characterized by a joint probability density function (PDF). When this detailed knowledge is unavailable or impractical, a weighted least squares cost function is often used. Typically the minima of the PDF cannot be solved for in closed form, and is therefore found by iterative search techniques.

Forward models have significant benefits over other reconstruction techniques, including known optimality properties, ability to tolerate incomplete and noisy data, and computation of Cramér-Rao bounds. They provide a straightforward approach to factor the complexities of real sensors and environments into the estimation process. The primary disadvantage of forward models is their computational complexity; however, modern computers and algorithms have largely mitigated this disadvantage. Another challenge can be occurrence of multiple minima in the cost function which can make finding the global minima difficult or impractical, in turn resulting in sub-optimal solutions that can depend on the initial estimates of the free parameters. Forward models naturally address several

challenges in intensity interferometry: complex non-linear relation of measurements of the object's squared Fourier magnitude to a spatial domain representation of the object, sparse and irregular spacing of the measurements in the Fourier plane, and low SNR. Forward models also offer the potential for computation of Cramér-Rao bounds (CRBs) [23]. CRBs are of special interest for intensity interferometry and other forms of image formation because they indicate fundamental statistical limits to image reconstruction performance and can be adapted to include the effects of constraints and biases [23-32].

This paper develops a forward model approach for image reconstruction from interferometric data. The resulting algorithm is referred to as FIIRE (Forward model Interferometry Image Reconstruction and Estimation). Section 2 describes the forward model which includes treatment of effects of finite aperture and spectral bandwidth (BW) on broadening the Fourier domain measurement response function beyond the idealized delta response. Section 3 describes the maximum *a posteriori* (MAP) cost function and the iterative search approach. Section 4 describes a conceptual intensity interferometry imaging system that represents the extreme of current feasibility and Section 5 characterizes the SNR it might achieve on a geosynchronous satellite. Section 6 investigates image reconstruction quality as a function of measurement SNR. Section 7 summarizes the conclusions.

2. FORWARD MODEL

Intensity interferometry operates by capturing light at two or more telescopes and combining the signals. The vector separation between a pair of telescopes, projected into the plane orthogonal to a line between the array and the object, is termed the baseline. Light collected at baseline vector $\bar{B}$ and wavelength λ provides information about the Fourier transform at spatial frequency $\bar{u} = \bar{B}/\lambda$. For conciseness, in the remainder of this document the Fourier domain will be referred to as the UV plane, and a measurement of the value of the object's Fourier transform will be referred to as a UV sample or visibility. In amplitude interferometry the light from the telescopes is optically interfered allowing measurement of both the UV amplitude and phase, also referred to as the complex visibility [33]. In phase closure techniques, appropriate products of complex UV samples from three or more baselines are formed which cancel out the effects of phase fluctuations from atmospheric turbulence and the collection system [34,35]. In intensity interferometry the fluctuations of the intensity of the light are measured at very high bandwidth. The normalized correlation of the fluctuations of the signals from two telescopes provides a direct measurement of the magnitude squared of complex visibility, hereafter referred to as visibility-squared denoted $|V|^2$ [2,33]:

$$|V|^2 \left(\bar{u} = \frac{\bar{B}_{k,k\prime}}{\lambda} \right) = \frac{\langle \Delta I_k(t,\lambda) \, \Delta I_{k\prime}(t,\lambda) \rangle}{\langle I_k(t,\lambda) \rangle \langle I_{k\prime}(t,\lambda) \rangle} \tag{1}$$

where t is time, λ is wavelength, telescope positions are indexed by k, I is intensity, Δ indicates fluctuations about the mean and $\bar{B}_{k,k\prime}$ is the baseline formed by telescope positions k and k'.

To make the forward model as general as possible the core code does not assume any particular geometry of the telescope array configuration. Its inputs are a list of measurements, each specified by UV coordinate and noise standard deviation. The FIIRE code can accept any mixture of complex visibility and $|V|^2$ measurements, the set of UV coordinates for each need not match nor have any regular spacing, they are completely arbitrary for each sensing modality. FIIRE has been designed with placeholders to expand its capability to utilize amplitude only and phase closure measurements. However, the focus of this paper is limited to intensity interferometry.

Under the conditions of negligible detector dark current, the measurement noise for a single intensity interferometry $|V|^2$ measurement is [4],

$$\sigma_{|V|^2} = \frac{1}{\sqrt{T \, \Delta f / 2}} \frac{\chi(\rho_T(\lambda) + \rho_B(\lambda))}{\rho_T^2(\lambda)} \tag{2}$$

where T is the collection time over which the signals are correlated, Δf is the detector BW, ρ_T and ρ_B are the signal levels of the light from the target and any background sources in photo-electrons per second per spectral bandwidth (Hz), and χ is the excess noise factor of the detector. The photon rate spectral densities are proportional to target and background brightness, telescope aperture area, transmission of the optical system, and detector quantum efficiency. This expression is accurate under conditions of low-degeneracy [33], which is satisfied by

direct or reflected thermal sources in the optical regime except at extraordinarily high temperatures, and detector response BW much smaller than spectral BW of the light. Note that the noise is dependent on the spectral density of the light only, so once the spectral BW significantly exceeds Δf there is no gain in SNR by detecting a larger spectral BW. If multiple measurements are collected such that their wavelengths and baselines map to UV coordinates with separations small compared to the correlation length of the complex spectrum, it simplifies things at no disadvantage to average them together to form a single input to image reconstruction processing. The spectrum correlation length is given by $\Delta u_{cor} \sim 1/W_{Obj}$, where W_{Obj} characterizes the width of the object. The highest reduction in noise is achieved by setting the weights equal to the reciprocal of the noise variances of the individual measurements, e.g. $w_m = 1/\sigma_m^2$. The effective noise standard deviation of the combined measurement is:

$$\sigma_C = \frac{\sqrt{\sum_j w_m^2 \, \sigma_m^2}}{\sum_m w_m} = \frac{\sqrt{\sum_m 1/\sigma_m^2}}{\sum_m 1/\sigma_m^2} = \frac{1}{\sqrt{\sum_m 1/\sigma_m^2}} \tag{3}$$

If the variances of all the measurements are similar this results in the standard $\sqrt{N}$ type noise reduction.

Now the object spatial intensity distribution needs to be related to the UV samples. In the ideal case a $|V|^2$ measurement samples a discrete point of the magnitude squared of the object's Fourier transform. However, as illustrated in Fig. 1(a), two telescope apertures actually measure light over a continuum of baselines because of their finite size. The measurement is an integral over the object's $|V|^2$ spectrum, with a weighting function equal to the autocorrelation of the aperture's transmission function. For a circular aperture of diameter D, the width of the UV footprint of the weighting function is $2D/\lambda$. The spectral BW of the signal causes a similar broadening, described by:

$$|\Delta u| = \left(\frac{1}{\lambda_{min}} - \frac{1}{\lambda_{max}}\right)|\bar{B}| = (\gamma_{max} - \gamma_{min})|\bar{B}| = \Delta\gamma|\bar{B}| \tag{4}$$

where the weighting function is now a line segment of length $|\Delta u|$ extending in a radial orientation from the UV plane origin, and $\Delta\gamma$ is the spectral BW in m^{-1}. For small spectral BWs and moderate apertures sizes the composite of the two effects is well approximated by their convolution. The resulting UV domain measurement response function, hereafter referred to as the UVPSF, is illustrated in Fig. 1(b):

$$D_j = \int d\bar{u} \, \left|\tilde{O}(\bar{u})\right|^2 UVPSF_j(\bar{u}) \tag{5}$$

$$UVPSF_j(\bar{u}) = \int_{\lambda_{j,min}}^{\lambda_{j,max}} d\lambda \, \{A \otimes A\}\left(\frac{\bar{u}}{\lambda}\right) \tag{6}$$

where j denotes a particular measurement, $A(\bar{x})$ is the transmission function of the telescope aperture, $\otimes$ denotes correlation, and $\lambda_{j,min/max}$ are the spectral range of the measurement. An object's UV spectrum is correlated over distances of $|\Delta u|\sim 1/\Omega$ where Ω is its angular subtense. It is desirable for the UVPSF to be much smaller than this width.
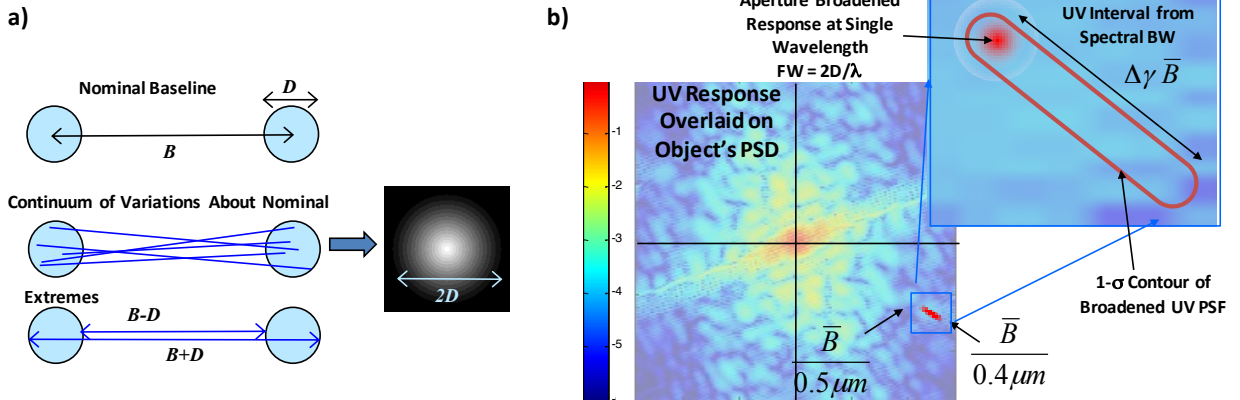
Fig. 1. (a) Illustration of UVPSF broadening due to finite aperture size of a telescope pair sensing light at a continuum of baselines. (b) Illustration of an aperture and spectrally broadened UVPSF overlaid on a logarithmic scale display of an object's UV spectrum.

The FIIRE forward model approximates the integral in Eq. (5) as follows. The object is represented as a grid of spatial domain values. It is transformed into the UV domain by the discrete Fourier transform (DFT). UV domain quantities are represented on the rectilinear grid of samples corresponding to object's DFT which is hereafter referred to as the UV grid. The values of the UV PSF for each measurement j are calculated on the UV grid using a discrete approximation to Eq. (6). Each UV PSF$_j$ is lexicographically ordered into a row vector, and these are stacked into a single matrix, R. The size of this matrix can be very large, however, typically only a tiny fraction of the elements of each row are non-zero. Using sparse matrix representation techniques (a basic capability of MatLab) solves the data storage issue. The forward model for the noiseless measurement is now simply expressed as

$$\bar{g} = R\,F\,|\bar{o}|^2 \tag{7}$$

where $\bar{o}$ is a lexicographical ordering of the elements of the spatial domain representation of the object intensity distribution, F denotes the DFT operation, and $\bar{g}$ is the vector of noiseless measurements. In code it is more efficient to calculate $F\,|\bar{o}|^2$ by a 2D FFT then re-order the result into a vector. With R pre-calculated, the forward model operation is extremely efficient. The forward model for amplitude interferometry is nearly identical but with $|\bar{o}|^2$ replaced by $\bar{o}$ in Eqs. (5) and (7). The case of UVPSFs that are smaller than UV grid spacing is currently treated by setting the values of R to be equivalent to bilinear interpolation. The code contains a placeholder to switch to sinc interpolation, which by the Fourier sampling theory is rigorously consistent with the physics. Truncating the sinc function to moderate size remains accurate yet still allows R to be highly sparse.

3. COST FUNCTION AND SEARCH ALGORITHM

The cost function is given in Eq. (8). It consists of a data agreement metric, shown as the first term, followed by five regularizing terms.

$$E = \sum_j^J \frac{1}{\sigma_j^\alpha} \left| \left|M_j\right|^\beta - \left|g_j\big(\hat{o}(\bar{x})\big)\right|^\beta \right|^\alpha \; - K_{Ent}\sum_{\bar{x}} \hat{o}(\bar{x})log\big(\hat{o}(\bar{x})\big) \; - K_{Tik}\sum_{\bar{x}} |\hat{o}(\bar{x})|^2$$

$$+ K_{TV}\sum_{\bar{x}} \left(|\nabla_{\mathrm{x}}\hat{o}(\bar{x})|^2 + \left|\nabla_{\mathrm{y}}\hat{o}(\bar{x})\right|^2\right)^{1/2} + K_{PSD-1D}\sum_n \left| \frac{\frac{1}{N_n}\sum_{\bar{u}\in S_n}\left|\hat{o}(\bar{u})\right|^2}{PSD(|\bar{u}|_n)} - D \right|^\xi \tag{8}$$

$$+ K_{PSD-2D}\sum_{\bar{u}} \left| \frac{\left|\hat{\hat{o}}(\bar{u})\right|^2}{PSD(|\bar{u}|_n)} - D \right|^\xi$$

In Eq. (8), $\hat{o}(\bar{x})$ is the estimate of the object and $\hat{\hat{O}}(\bar{x})$ its DFT, M_j denotes a noisy measured value and $g_j\big(\hat{o}(\bar{x})\big)$ its prediction based on the object estimate and forward model, derivatives of the object in the x and y directions are indicated by ∇_{x} and ∇_{y}. The agreement metric compares the discrepancy between the measurements and their predicted values. The discrepancy is quantified as an L-α norm, where α is between 1 and 2. There is also a shaping exponent, β, which can increase sensitivity to small values of the measured data. The measurement terms are individually weighted according to their respective variances σ_j^2. As described in more detail below, the constant D in the final two terms controls whether they act purely as smoothness constraints by penalizing non-zero Fourier values, or act to encourage reconstructions to be consistent with *a priori* expectations about the object's power spectral density (PSD).

The regularizing terms in Eq. (8) each serve different functions. The entropy term, with leading factor K_{Ent}, acts to smooth the object and encourage the energy of the object to be contained in a smaller number of pixels or equivalently discouraging small amounts of energy in many pixels. The Tikhonov or image sharpness regularization term, with leading factor K_{Tik}, tends to concentrate energy in a limited number of pixels. The next term in Eq. (8) is the total variation term, with leading factor K_{TV}. This well known regularizing approach serves to suppress noise

while preserving sharp edges. There is not currently any provision for optimizing the relative weights of each term, this is left to the user. The term with leading factor K_{PSD-1D}, imposes prior information in terms of the expected PSD as a function of radial distance of a UV coordinate from the origin, e.g. $|\bar{u}|$. This is accomplished by dividing the UV domain into a series of concentric annuli, with S_n specifying the set of N_n UV grid elements in annulus n, and $|\bar{u}|_n$ characterizing the annulus' radius. The average of the object estimate's PSD values within an annulus is calculated and divided by the expected PSD. When D takes the value 1, this term encourages the estimated object to be consistent with expectations about its power spectrum. When D equals 0, this term encourages object smoothness by incurring a penalty for larger PSD values, with the penalty at a spatial frequency weighted by the inverse of the *a priori* PSD. Since the PSD in the denominator is the average *a priori* PSD as function of $|\bar{u}|_n$ it does not express any assumptions about the object's rotational orientation.

This cost function can be extended to incorporate data from other sensing modalities such as amplitude interferometry, phase closure, and conventional imaging by adding additional data agreement cost terms for each modality analogous to the 1st term in Eq. (8). This enables joint processing of all data to find an object solution that is in balanced agreement with all data sources and the regularizing priors, while also subject to non-negative and an optional support constraint.

A solution for the grid of object intensity values that minimizes the cost function is sought using the L-BFGS-B iterative limited memory quasi-Newton search algorithm [36]. As it searches through parameter space L-BFGS-B accelerates the search by developing an approximate model of the local 2nd order partial derivatives without requiring evaluation or storage of the full Hessian matrix. It also has provisions for placing upper and lower bounds on each parameter providing a direct approach to enforcing the non-negative property of the object. The FIIRE code allows this option or alternatively a re-parameterization of the object as the square of an underlying function which also has the effect of ensuring non-negativity. Support constraints are easily employed by limiting the set of object grid elements which are optimized and leaving the rest at zero. This approach requires calculations of the gradients of the cost function with respect to the object; closed form expressions for each term in Eq. (8) are easily calculated but not shown here. Use of Eq. (7) allows the efficient simultaneous computation of all elements of the gradient of the 1st term of Eq. (8), the data agreement term, using FFTs and matrix multiplies. One other regularization technique supported by FIIRE that should be mentioned is to re-parameterization the object as the convolution of a low-pass kernel with an underlying function. This has been referred to as the method of sieves [38] and effectively places a support constraint on the object estimate's UV spectrum preventing amplification of high-frequency noise. If the transfer function corresponding to the Fourier transform of the kernel decreases with increasing $|\bar{u}|$ then it will act to attenuate the convergence of higher frequency components which can help to avoid local minima. It should be noted that the algorithmic approach used by FIIRE is quite similar to that of MIRA [22, 34], another image reconstruction code widely recognized in the imaging interferometry community [38].

4. INTENSITY INTERFEROMETRY SYSTEM

To demonstrate the FIIRE code and investigate influence of its various features on reconstructed image quality, an intensity interferometry collection system was defined based on the Cherenkov Telescope Array (CTA) which is comprised of 97 telescopes arranged on a 1 km wide square. This system is described in detail in reference [39]. Note the pattern of telescope positions is chosen to give a higher diversity of baselines than would a pattern with equal spacing. Nevertheless, many of the telescope pairs have equivalent baselines resulting in considerable redundancy in the UV measurements especially at smaller separations. Since an emphasis of this study was to investigate ground-based imaging of objects in geosynchronous Earth orbit (GEO), the square pattern of telescope positions was scaled down to 40 m across which is better matched to the angular subtense and desired angular resolution. Fig. 2 shows the geometry of this array and the resulting baselines assuming a zenith line-of-sight. Color-coding indicates the level of redundancy at each baseline. The main details of the system parameters are summarized in the following list:
- 97 telescopes arranged within a 40×40 m square providing 653 unique baselines
- 0.75 m diameter apertures with 0.375 m diameter central obscurations for .3313 m^2 collection area
- 0.196 net system transmission (atmosphere * optics * quantum efficiency)
- Nyquist sampling for maximum horizontal baseline is 5 nrad (7.3E-4 arcsec), corresponding to 17.9 cm at GEO

- Light is detected in 84 spectral channels spanning 400-900 nm
- The channels are evenly spaced in wavenumbers at 0.0167 μm^{-1} and each is 0.0083 μm^{-1} wide. This comprises 50% utilization of the full 400-900 nm spectrum.
- Each channel is divided into 25 contiguous sub-channels of 100 GHz width and spacing
- Light in each sub-channel is measured with a 500 MHz BW detector and 1 GHz sample rate

Figure 3 diagrams the division of the broad spectrum into channels and sub-channels. Physical methods of achieving this were not a focus of this investigation, but a potential approach that could accurately separate the channels at the necessary spectral resolutions is use of Echelle cross-grating spectrometers combined with micro-lens assemblies to collect and couple the light into optical fibers fed into high BW detectors. The goal of dividing up the spectrum is to gain best advantage of the full visible band of light. Consider a large satellite of 40 m maximum width at a range of 40,000 km. This corresponds to an angular subtense of 1 μrad. Nyquist sampling of its UV spectrum is $\Delta u = 1$ μrad^{-1}. By Eq. (1), at the maximum baseline of 40 m, a spectral channel of 0.048 μm^{-1} BW maps to a line-segment on the UV plane of length 0.27 μrad^{-1} thus is significantly smaller than the correlation length of the object's UV spectrum and can be treated as nearly a point sample such that UVPSF effects are not a concern. On the other hand, at 400 nm the 0.75 m aperture diameter results in a UV PSF width of 3.75 μrad^{-1} and could cause problematic blur of the UV measurements. To get higher utility of the light within a channel it is divided into 25 contiguous sub-channels that are separately measured. Each pair of matching sub-channels collected by a pair of telescopes is correlated, then each set of $|V|^2$ measurements within a channel are averaged to boost the SNR by $\sqrt{25}$. This partially compensates for the restriction that SNR is limited by the BW of the detector response not the BW of the detected light. Fig. 4 shows the resulting set of UV sample locations of the described system color-coded by their wavenumber.
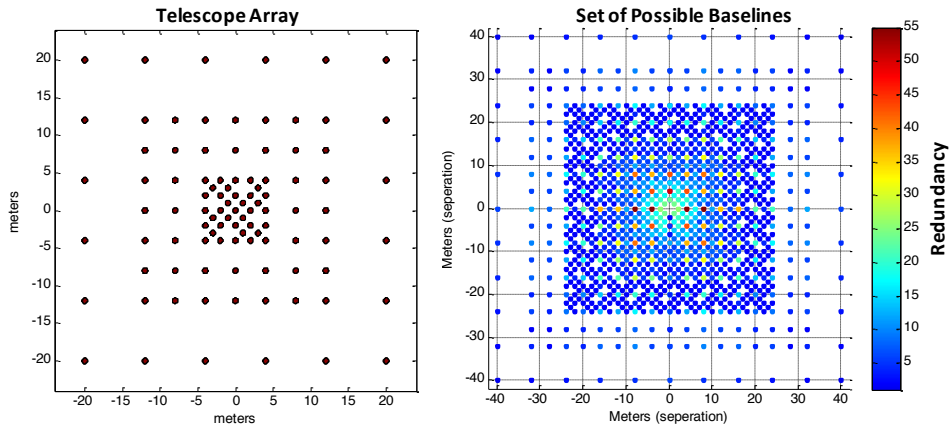

Fig. 2. Telescope array geometry and corresponding set of baselines for the analyzed intensity interferometer system.
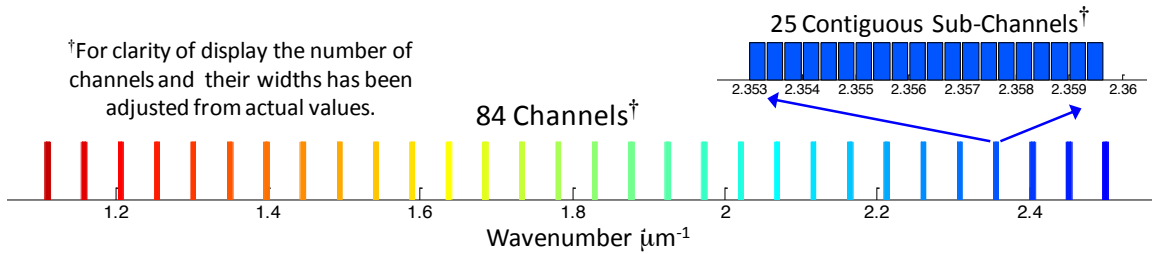

Fig. 3. Division of broadband light into channels and sub-channels.

- **653 unique baselines**
- **84 spectral channels**
- **54,852 UV samples map to 4905 distinct object UV correlation cells**
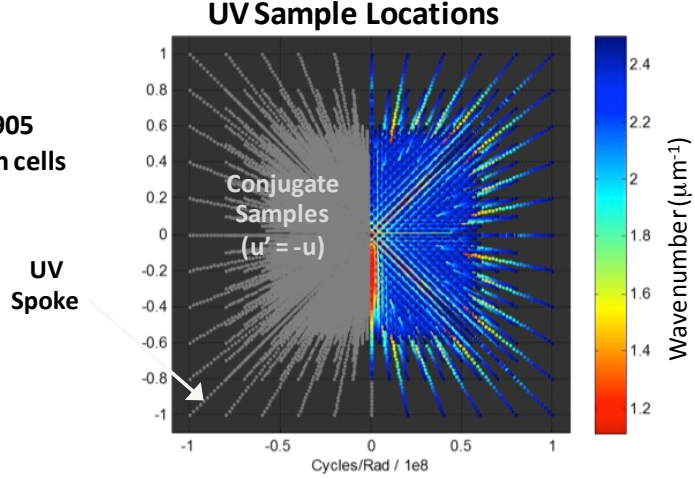- **Compare to 40,000 pixels for 256x256 image**

Fig. 4. Set of UV samples collected by the described system color-coded by wavelength.

It is worth some comments about the challenges for the discussed system. By dividing the spectrum into 84 channels, each comprised of 25 sub-channels, each of the 97 telescopes would require 2100 high BW detectors, thus 203,700 for the full system. To ensure the spectral BW of matching sub-channels from different telescopes overlap by at least 90% will require exquisite spectral accuracy of 10 GHz which corresponds to 5 picometers at the 400 nm end of the spectrum. With 4656 telescope pairings, to avoid storing the 203E+3 giga-samples/sec of data that is generated will require approximately 10 million correlators. This design was chosen to be representative of what at the time of this paper is an achievable, but large, complex, and costly system.

5.   Visibility SNR

Photo-electron signal level is now considered. The photon flux at the top of the atmosphere for a M_v 10 object is illustrated in the left-hand plot of Fig. 5 as a function of wavelength [40]. Assuming a clear-aperture area of 0.3313 m^2 and net transmission efficiency of 19.6% including atmosphere, optics, and quantum efficiency, results in a spectral density of about 7E-10 photo-electrons per second per Hz. Photo-electron rate spectral density is plotted vs. wavelength in the right-hand plot of Fig. 5.
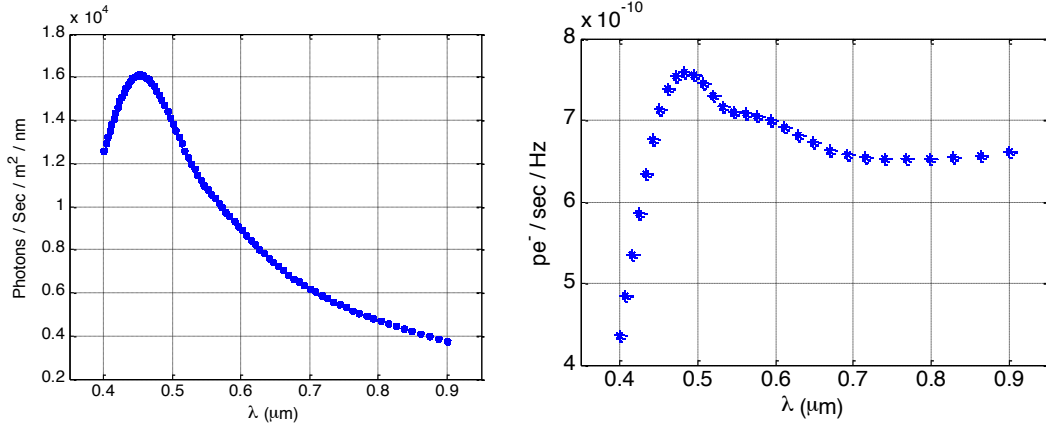

Fig. 5. Top-of-atmosphere photon flux from a M_v 10 object (left), and resulting photo-electron spectral density at the detector (right).

An individual measurement is defined as the correlation between two sub-channels which for a 1 hour integration time and signal level of 7E-10 pe-/sec/Hz results in a $|V|^2$ noise standard deviation of ~1500. It simplifies the processing at no loss to combine individual measurements that are close together relative to the UV spectrum's

correlation length by averaging them weighted by the inverse of their variances. This was accomplished in this study by grouping individual UV measurements into sets such that all members in a set lied within 0.375 * Δu_{cor} of each other. The SNR of each resulting composite UV sample j is defined

$$SNR_{|V|_j^2} = \frac{|\tilde{O}(\bar{u}_j)|^2}{\sigma_{C,j}} \tag{9}$$

where $\sigma_{C,j}$ is defined by Eqs. (2-3). The average number of individual measurements per composite UV sample was ~2000 resulting in an average value of σ_C of 77 which is a factor of 20 improvement compared to the noise of the individual constituent samples. The noise level $\sigma_{C,j}$ and SNR will vary for different composite UV samples $\bar{u}_j$ for a number of reasons, (a) variations in the level of redundant telescope pairings with same baseline, (b) variations in the number of baseline and wavelength combinations mapping to a particular $\bar{u}_j$, (c) variations of photon flux at different wavelengths, (d) variations in the object's UV spectrum $|\tilde{O}(\bar{u})|^2$ which for most objects will tend to follow a power-law type decrease $|\bar{u}|^{-\alpha}$. Panels (b-c) of Fig. 6 show a histogram of the values of $\sigma_{C,j}$ and characterize the variations with $|\bar{u}_j|$. By Eq. (2) noise standard deviation scales inversely to the square-root of the collection time.

To further characterize SNR it is useful to consider a specific object. The pristine intensity distribution shown in Fig. 7(a) was generated from a 3D model and is placed at a range of 35.8E+3 km. This object will also be used for image reconstruction analysis in Section 7. Fig. 7 also shows (b) the object's PSD, (c) the set of UV sample locations measured by the system described in Section 2, and (c) the image collected by a conventional full-aperture telescope with diameter such that its modulation transfer function (MTF) cutoff matches the UV sample with the largest radius indicated by the red circle in (d). Fig. 6 provides several plots characterizing the distributions of $|V|^2$, noise, and SNR, and their trends with UV coordinate radius $|u|$ for a 1-hour signal collection time. Per Eq. (2) SNR will scale in proportion to the square-root of the collection time. It is observed that noise level tends to be higher for larger $|u|$ which results from the array geometry providing fewer redundant telescope pairs at longer baselines. Combined with a rapid decrease in $|V|^2$ at higher spatial frequencies, SNR drops rapidly with increasing $|u|$. Fig. 6(f) indicates that for a 1-hour collection time the bulk of the UV samples have SNRs between 10^{-6} to 10^{-4}.
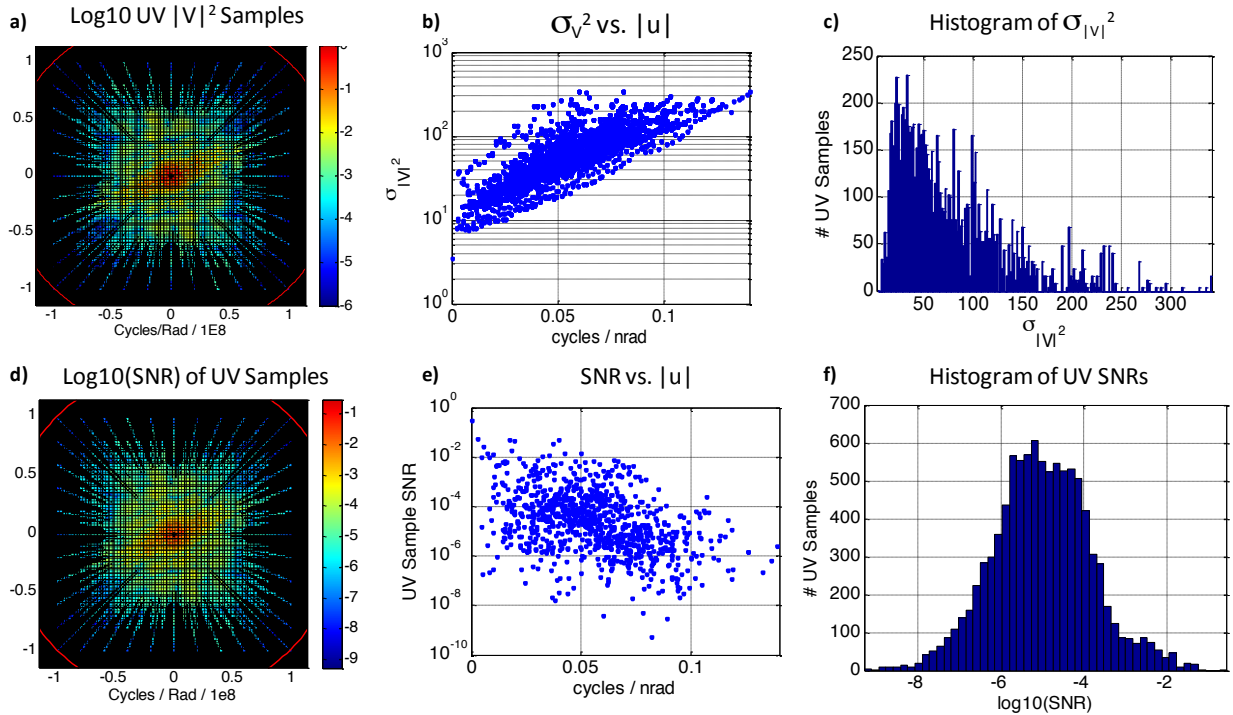

Fig. 6. Plots characterize $|V|^2$ magnitudes, noise, and SNR levels and their trends vs. radial distance from UV origin based on a 1-hour signal collection time for the satellite object of Fig. 7 at M_v=10 brightness.
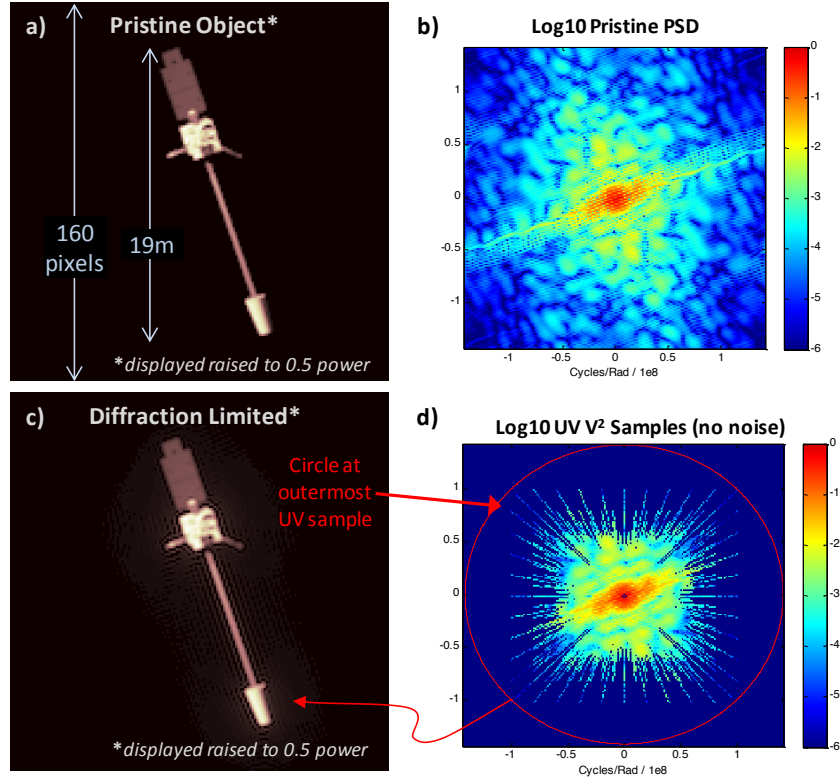
Fig. 7. (a) Pristine object; (b) object's PSD; (c) diffraction limited image from full aperture telescope with MTF cutoff matching highest UV sample; (d) UV sample positions.
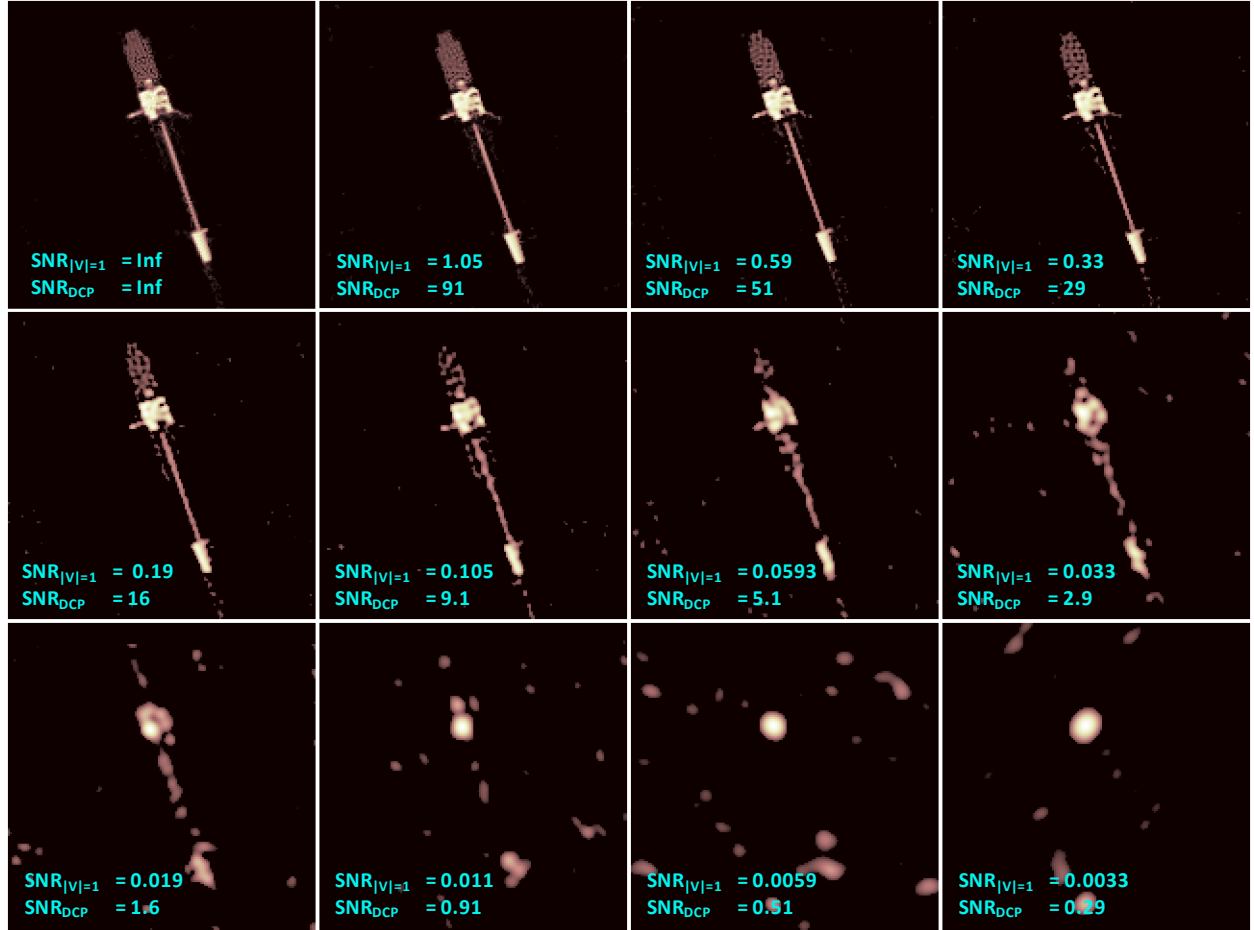
6.   IMAGE RECONSTRUCTION ANALYSIS

6.1 Image Quality vs. SNR

This section examines reconstructed image quality dependence on SNR of the $|V|^2$ measurements. The test object and interferometry system are as described in Sections 4 and 5. Reconstructions were performed using the FIIRE code. The simulation parameters are summarized in the following list:
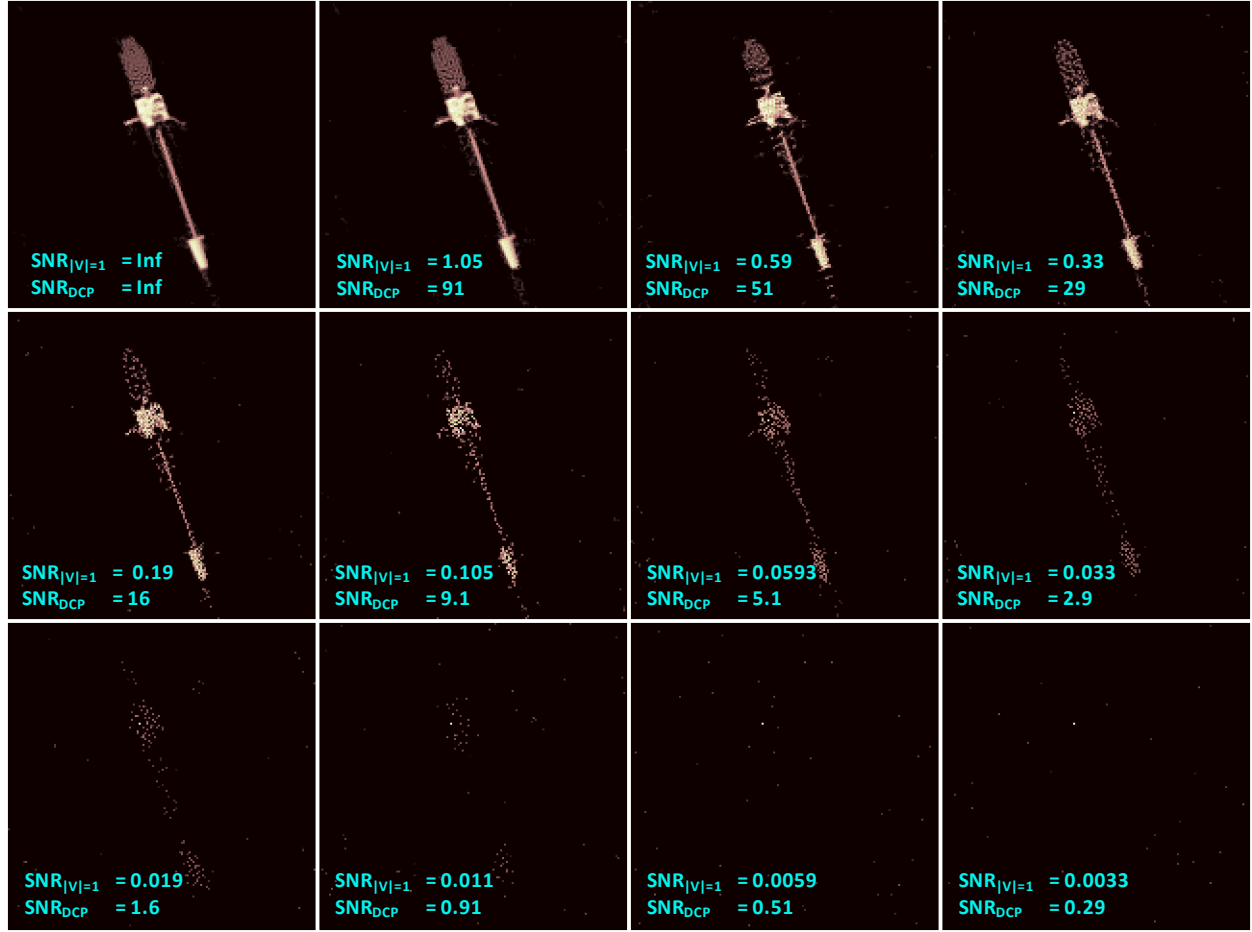
- The object was estimated on a 256×256 grid corresponding to a 40×40 meter FOV, exactly matching the grid the original pristine object used to simulate the $|V|^2$ measurements is represented on
- Iterations were performed until convergence to numerical tolerance or a maximum 8,000 iterations
- The UVPSD was set to a delta function, i.e., spectral and aperture induced broadening were not modeled
- Initial estimate was a Gaussian spatial distribution multiplied by white noise
- Object non-negativity was enforced but a support constraint was not used

- Earth rotation was ignored, so the orientation of the telescope array relative to the object was treated as fixed over the observation time
- Images were generated using each of the different regularization terms activated one at a time. Combinations were not explored. For each term the regularization weight was scanned over a large range of values to determine an optimum strength. The 1D PSD term with D=1 (i.e., discrepancy not penalty) was found to produce the best results (visually). A weight of 1E-3 was found to be optimum for all cases except infinite SNR at which point a weight of 1E-5 was better.

Figure 8 shows the image reconstructions obtained for a range of measurement SNR levels. Note that lack of phase information results in an ambiguity such that a solution and its 180° rotation are equivalent. For purposes of display the reconstructions were rotated to match the pristine object as necessary. Two SNR metrics are annotated on each image. $SNR_{|V|=1}$ is calculated from Eqs. (2-3) using the average of the 25 sub-channels provided by a single channel from a single telescope pair with $|v|^2=1$, e.g. the object's normalized PSD value at the origin of the UV plane, or equivalently unity coherence between the intensity fluctuations. For a 1 hour integration time, $SNR_{|V|=1}=0.0033$. The peak SNR for the UV samples is characterized by $SNR_{DCP} \equiv 88*SNR_{|V|=1}$ and corresponds to the SNR at $|V|=1$ for the composite UV sample with lowest noise standard deviation. It is observed that the basic dumbbell structure of the object starts to become discernible at $SNR_{DCP} = 1.6$. More detailed features start to appear as SNR_{DCP} exceeds 5. Near diffraction-limited quality is achieved at $SNR_{DCP} = 29$. Figure 9 is similar to Fig. 8 but with the reconstructions performed without any regularization. It is obvious that regularization is effective in suppressing meaningless high-frequency structure to produce an image with more pleasing appearance. It is debatable whether they are better from the standpoint of the information visually conveyed, but the suppression of false high-frequency structure may likely benefit automated information extraction methods.

For improved clarity images are displayed with dynamic range thresholding and gamma adjustment

Fig. 8. Image reconstruction results for a range of SNR levels.

SNR$_{	V	=1}$ = Inf	SNR$_{	V	=1}$ = 1.05	SNR$_{	V	=1}$ = 0.59	SNR$_{	V	=1}$ = 0.33
SNR$_{DCP}$ = Inf	SNR$_{DCP}$ = 91	SNR$_{DCP}$ = 51	SNR$_{DCP}$ = 29
SNR$_{	V	=1}$ = 0.19	SNR$_{	V	=1}$ = 0.105	SNR$_{	V	=1}$ = 0.0593	SNR$_{	V	=1}$ = 0.033
SNR$_{DCP}$ = 16	SNR$_{DCP}$ = 9.1	SNR$_{DCP}$ = 5.1	SNR$_{DCP}$ = 2.9
SNR$_{	V	=1}$ = 0.019	SNR$_{	V	=1}$ = 0.011	SNR$_{	V	=1}$ = 0.0059	SNR$_{	V	=1}$ = 0.0033
SNR$_{DCP}$ = 1.6	SNR$_{DCP}$ = 0.91	SNR$_{DCP}$ = 0.51	SNR$_{DCP}$ = 0.29

For improved clarity images are displayed with dynamic range thresholding and gamma adjustment

Fig. 9. Same as Fig. 8 but without regularization.

6.2 Optimal Telescope Array Scaling

Figure 10 compares reconstructions obtained with the telescope location pattern scaled to 1, ½, and ¼ that of Fig. 2. Telescope aperture area was held fixed. The middle reconstruction corresponding to ½ scale appears the best. The rightmost is clearly worse and though the left reconstruction contains finer structures, they do not correlate with fine-scale features in the pristine image and are just amplified noise. This suggests there is benefit to optimizing the array pattern to match the characteristic width of the object, such that the density of samples and levels of SNR-boosting redundancy are concentrated where they are most useful.
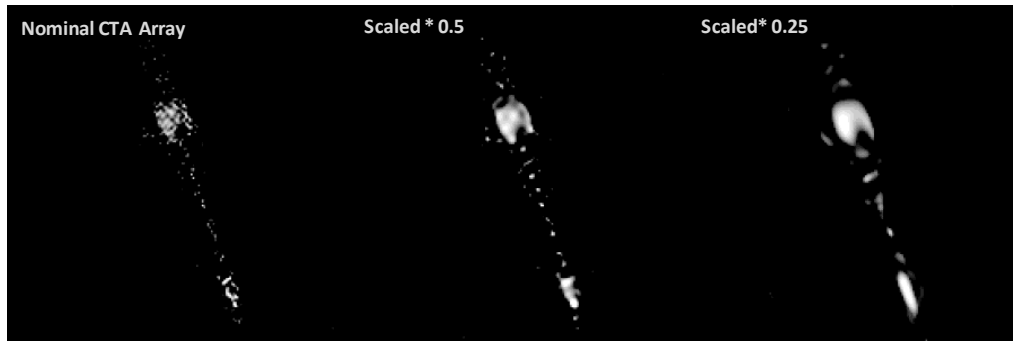

Fig. 10. Image reconstructions vs. different scaling of the telescope array pattern.

6.3 UV Sample Weighting

Three choices for specifying the UV sample variances, σ_j^2, used in the 1st term of the cost function expressed by Eq. (8) were explored. The first was to use the true variances of the noise added in simulating the visibility measurement data defined by Eqs. (2-3), which matches the measurement physics and method of combining redundant samples given by Eq. (3). The second method was to scale these by a multiplicative factor. The third was to use an identical value for all UV samples. The third method led to much worse performance than the other methods. Variations in image reconstruction quality were imperceptible for scale factors between $0.001 - 1000$ beyond which quality began to degrade.

7. SUMMARY

A code was developed for reconstructing images from long-baseline interferometry data based on a forward model approach in which an object is estimated such that when propagated through a physics-based forward model of the sensing system maximizes the match to the set of measurements. The code currently supports joint processing of complex amplitude and $|V|^2$ type measurements. Explorations of different regularization methods and measurement weighting schemes gave insights into the approaches that were reliably best. It was observed that scaling the telescope array location pattern to match the resulting UV measurement location and SNR distribution to the PSD of the object was important to maximizing image quality. The performance of a conceptual system representing the extreme of what might be achieved with current technology was considered. The system consisted of an array of 97 telescopes, each with a 0.75 m diameter aperture using 2100 narrowband spectral channels spread across 400-900 nm to make highly efficient use of the photons within the visible band. Signals from all 4656 pairings of telescopes were correlated to gain the full Fellgett's advantage of the system. The array pattern and wide spectral bandwidth resulted in many measurements of nearly identical UV locations, which were averaged using a scheme that resulted in a typical number of many hundred redundant measurements per UV locations. Taking the SNR benefit from this redundancy into account, for a M_v 10 object and UV location with $|V|^2 \approx 1$, it was determined that an SNR$_{DCP}$ of approximately 2 was needed to recover the coarse structure of the object. With the described system this would take at least 1000 hours of integration time. Finer details of the object started to appear as SNR$_{DCP}$ exceeded 5, with image quality increasing steadily up to SNR$_{DCR}$~30 at which point a near diffraction-limited quality image was obtained. This study suggests that in principle intensity interferometry could produce images of GEO objects. However at typical GEO object brightness levels, major advances in measurement technology or algorithmic approaches will be needed to achieve images with reasonably small collection times. It will be interesting to see how this picture changes with use of other interferometric techniques such as amplitude interferometry.

8. ACKNOWLEDGEMENT

9. REFERENCES

1. R. Hanbury Brown, R. C. Jennison, and M. K. Das Gupta, "Apparent angular sizes of discrete radio sources: observations at Jodrell Bank, Manchester," Nature **170**, 1061-1063, 1952.
2. R. Hanbury Brown and R. Q. Twiss, "Interferometry of the intensity fluctuations in light; I. Basic theory: the correlation between photons in coherent beams of radiation," Proc. R. Soc. Lond. A **242**, 300-324, 1957.
3. R. Hanbury Brown and R. Q. Twiss, "Interferometry of the intensity fluctuations in light; II. An experimental test of the theory for partially coherent light," Proc. R. Soc. Lond. A **243**, 291-319, 1958.
4. R. Hanbury Brown, *The intensity interferometer – its application to astronomy*, Taylor & Francis, London (1974).

5. M. L. Goldberger, H. W. Lewis, and K. M. Watson, "Use of intensity correlations to determine the phase of a scattering amplitude," Phys. Rev. **132**, 2764-2787, 1963.

6. R. Q. Twiss, "Applications of intensity interferometry in physics and astronomy," Optica Acta **16**, 423-451, 1969.

7. P. R. Fontana, "Multidetector intensity interferometers," J. Appl. Phys. **54**, 473-480, 1983.

8. E. M. Vartiainen, K. Peiponen, and T. Asakura, "Phase retrieval in optical spectroscopy: resolving optical constants from power spectra," Appl. Spec. **50**, 1283-1289, 1996.

9. J. Baldwin, M. Beckett, R. Boysen, D. Burns, D. Buscher, G. Cox, C. Haniff, C. Mackay, N. Nightingale, J. Rogers, P. Scheuer, T. Scott, P. Tuthill, P. Warner, D. Wilson, R. Wilson, "The first images from an optical aperture synthesis array: mapping of Capella with COAST at two epochs," Astron. Astrophys. **306**, L13-L16, 1996.

10. J. T. Armstrong, D. Mozurkewich, L. J Rickard, D. J. Hutter, J. A. Benson, P. F. Bowers, N. M. Elias II, C. A. Hummel, K. J. Johnston, D. F. Buscher, J. H. Clark III, L. Ha, L.-C. Ling, N. M. White, and R. S. Simon, "The Navy Prototype Optical Interferometer," ApJ **496**, 550—571, 1998.

11. T. A. ten Brummelaar, et al., "First results from the CHARA Array. II. A description of the instrument," ApJ. **628**, 453-465, 2005.

12. J. H. Seldin and J. R. Fienup, "Numerical investigation of the uniqueness of phase retrieval," J. Opt. Soc. Am. A. **7**, 412-427, 1990.

13. R. G. Lane and R. H. T. Bates, "Automatic multidimensional deconvolution," J. Opt. Soc. Am. A **4**, 180-188, 1987.

14. H. V. Deighton, M. S. Scivier, and M. A. Fiddy, "Solution of the two-dimensional phase-retrieval problem," Opt. Lett. **10**, 250-251, 1985.

15. D. Israelevitz and J. S. Lim, "A new direct algorithm for image reconstruction from Fourier transform magnitude," IEEE Trans. Acoust., Speech, Signal Proc. **ASSP-35**, 511-519, 1987.

16. R. G. Lane, W. R. Fright, and R. H. T. Bates, "Direct phase retrieval," IEEE Trans. Acoust., Speech, Signal Proc. **ASSP-35**, 520-525, 1987.

17. D. C. Ghiglia, L. A. Romero, and G. A. Mastin, "Systematic approach to two-dimensional blind deconvolution by zero-sheet separation," J. Opt. Soc. Am. A **10**, 1024-1036, 1993.

18. P. Chen, M. A. Fiddy, A. H. Greenaway, and Y. Wang, "Zero estimation for blind deconvolution from noisy sampled data," Proc. SPIE **2029**, 14-22, 1993.

19. P. J. Bones, C. R. Parker, B. L. Satherley, and R. W. Watson, "Deconvolution and phase retrieval with use of zero sheets," J. Opt. Soc. Am. A **12**, 1842-1857, 1995.

20. R. Holmes and M. Belen'kii, "Investigation of the Cauchy-Riemann equations for one-dimensional image recovery in intensity interferometry," J. Opt. Soc. Am. A **21**, 697-707, 2004.

21. T. J. Shulz and D. Voelz, "Signal recovery from autocorrelation and cross-correlation data," J. Opt. Soc. Am. A **22**, 616-624, 2005.

22. E. Thiébaut, "Image reconstruction with optical interferometers," New Astronomy Reviews **53**, 312–328, 2009.

23. S. Kay, *Fundamentals of Statistical Signal Processing: Estimation Theory* (Prentice Hall, New Jersey, 1993).

24. E. L. Lehmann and G. Casella, *Theory of Point Estimation* (Springer-Verlag, New York, 1998).

25. J. D. Gorman and A. O. Hero, "Lower bounds for parametric estimation with constraints," IEEE Trans. Inform. Theory **36**, 1285–130, 1990.

26. A. O. Hero III, J. A. Fessler, and M. Usman, "Exploring estimator bias-variance tradeoffs using the uniform Cramér–Rao bound," IEEE Trans. Signal Proc. **44**, 2026–204, 1996.

27. Charles L. Matson and Alim Haji, "Biased Cramér–Rao lower bound calculations for inequality-constrained estimators," J. Opt. Soc. Am. A **23**, 2702-2712, 2006.

28. B. Calef, "Quantifying the benefits of positivity," Proc. SPIE **5896**, 37-44, 2005.

29. Jonas Zmuidzinas, "Cramér–Rao sensitivity limits for astronomical instruments: implications for interferometer design," J. Opt. Soc. Am. A **20**, 218-233, 2003.

30. C. L. Matson, C. C. Beckner, and M. Flanagan, "A Cramér-Rao lower bound analysis of multi-frame blind deconvolution," AMOS Technical Conf. Proc., 2012.

31. C. L. Matson, M. Flanagan, and R. A. Vincent, "The impact of low signal-to-noise ratio values on the achievability of Cramér-Rao lower bounds with multi-frame blind deconvolution algorithms," Proc. SPIE **7828**, 2010.

32. C. L. Matson, "A comparison of multi--frame blind deconvolution and speckle imaging energy spectrum signal-to-noise ratios," Proc. SPIE **7108**, 2008.

33. J. Goodman, *Introduction to Fourier Optics*, (McGraw-Hill, New York, 1968).

34. E. Thiébaut and J.-F. Giovannelli, "Image reconstruction in optical interferometry," IEEE Sig. Proc. **97**, 2010.

35. T. J. Cornwell, "Radio-interferometric imaging of weak objects in conditions of poor phase stability: the relationship between speckle masking and phase closure methods," Astron. Astrophys. **180**, 269-274, 1987.

36. R. H. Byrd, P. Lu, and J. Nocedal, "A limited memory algorithm for bound constrained optimization," SIAM Journal on Scientific and Statistical Computing, **16**(5), 1190-1208, 1995.

37. D. L. Snyder and M. I. Miller, "The use of sieves to stabilize images produced with the EM algorithm for emission tomography," IEEE Trans. Nuc. Sci. **NS-32**(5), 3864-3872, 1985.

38. F. Malbet, et al., "The 2010 Interferometric Imaging Beauty Contest," Proc. SPIE **7734**, N1-12, 2010.

39. P. D. Nuñez, R. Holmes, D. Kieda, and S. LeBohec, "High angular resolution imaging with stellar intensity interferometry using air Cherenkov telescope arrays," Mon. Not. R. Astron. Soc. **419**, 172-183, 2012.

40. *The Infrared & Electro-Optical Systems Handbook, Vol 1, Sources of Radiation*, G. J. Zeiss Editor, p 168, (ERIM & SPIE, Bellingham, 1993).